An improved algorithm for unmixing first-order reversal curve diagrams using principal component analysis

Richard J. Harrison[1], Joy Muraszko[1], David Heslop[2], Ioan Lascu[3], Adrian R. Muxworthy[4], Andrew P. Roberts[2]

[1]Department of Earth Sciences, University of Cambridge, Downing Street, Cambridge, U.K.

[2]Research School of Earth Sciences, Australian National University, Canberra, ACT, Australia

[3]Department of Mineral Sciences, National Museum of Natural History, Smithsonian Institution, Washington, U.S.A.

[4]Department of Earth Science and Engineering, Imperial College, London, U.K.

Corresponding author: Richard Harrison (rjh40@cam.ac.uk)

Key Points:

- The FORC-PCA unmixing method is tested on synthetic mixtures of magnetic domain states.
- A new FORC-PCA algorithm is developed that solves the linear mixing problem for end members with different domain states (including superparamagnetism).
- Feasibility metrics are developed that help to guide identification of physically realistic end members.

Abstract

First-order reversal curve (FORC) diagrams of synthetic binary mixtures with single-domain, vortex state, and multi-domain end members (EMs) were analyzed using principal component analysis (FORC-PCA). Mixing proportions derived from FORC-PCA are shown to deviate systematically from the known weight percent of EMs, which is caused by the lack of reversible magnetization contributions to the FORC distribution. The error in the mixing proportions can be corrected by applying PCA to the raw FORCs, rather than to the processed FORC diagram, thereby capturing both reversible and irreversible contributions to the signal. Here we develop a new practical implementation of the FORC-PCA method that enables quantitative unmixing to be performed routinely on suites of FORC diagrams with up to four distinct EMs. The method provides access not only to the processed FORC diagram of each EM, but also to reconstructed FORCs, which enables objective criteria to be defined that aid identification of physically realistic EMs. We illustrate FORC-PCA with examples of quantitative unmixing of magnetic components that will have widespread applicability in paleomagnetism and environmental magnetism.

1. Introduction

Natural samples contain magnetic minerals with a wide range of grain sizes, domain states, coercivity distributions, anisotropies, and interaction fields. First-order reversal curve (FORC) diagrams provide a powerful method to characterize all these aspects of the magnetic mineralogy (Pike et al., 1999; Roberts et al., 2000; Roberts et al., 2014), although their interpretation in the literature is often based on qualitative assessments and empirical ‘fingerprinting’. Developments in theoretical modelling (Muxworthy et al., 2004; Newell, 2005; Egli, 2006; Harrison & Lascu, 2014; Roberts et al., 2017), new measurement protocols (Zhao et al., 2015, 2017), and new analysis methods (Egli, 2013; Egli & Winklhofer, 2014; Heslop et al., 2014) have placed the processing and interpretation of FORC diagrams onto a firm physical footing, which provides the opportunity for a more quantitative approach to rock magnetic characterization. Application of principal component

analysis (Jolliffe 2002) to analyze entire sets of FORC diagrams (FORC-PCA) was introduced by Lascu et al. (2015) as a quantitative method to unmix a suite of related samples into a linear combination of up to four end members (EMs). The method has been applied successfully to unmix the biogenic and detrital magnetic components of a sediment core from the Rockall Trough (Channell et al., 2016), to characterize glacial/interglacial sedimentation on the Northwest Iberian Margin (Plaza-Morlote et al., 2017), and to unmix the pedogenic and detrital magnetic components of Minnesotan soils (Maxbauer et al., 2017). The key advantage of FORC-PCA lies in the two-dimensional nature of the FORC diagram. Unmixing one-dimensional coercivity distributions (e.g., by fitting to the sum of standard basis functions) can be ambiguous, especially when there is strong overlap between the coercivity distributions of different components (Heslop, 2015). The information provided by the vertical B_u axis of a FORC diagram, however, provides additional sensitivity to the presence of superparamagnetic (SP), single-domain (SD), vortex (V), and multi-domain (MD) states, the ability to detect the presence or absence of interactions in each EM, and a way to discriminate between minerals with different types of magnetocrystalline anisotropy. Note that throughout this paper we follow Roberts et al. (2017) in referring to 'vortex' states rather than to 'pseudo-single domain' or 'PSD' states. The term 'vortex' is broadly defined by Roberts et al. (2017) to include both single-vortex (SV) and multi-vortex (MV) states, which more accurately describe the physics of magnetic particles (Donnelly et al., 2017) in the intermediate size range between the SD and MD states.

Despite the numerous advantages of FORC-PCA, the method has some shortcomings that currently limit its usefulness for rock magnetic characterization. First, the FORC distribution is sensitive primarily to the irreversible component of the magnetic response of a sample to a changing magnetic field. Purely reversible responses to the changing field (e.g., from superparamagnetic, paramagnetic, antiferromagnetic or diamagnetic sources), are strictly absent from the FORC diagram, and cannot be identified as EM components in a FORC-PCA analysis. Even for

ferrimagnetic sources, the magnetization response of any sample can be split into the sum of reversible and irreversible components, with the ratio of the two depending largely on the domain state: SD states are dominated by irreversible magnetization, whereas MD states are dominated by reversible magnetization. In its current form, therefore, the unmixing proportions reported by FORC-PCA may deviate significantly from the actual proportions (by mass or volume) of the EMs present in the sample, especially if the EMs represent populations of grains with different domain states. Second, the process of choosing appropriate EMs (based often on a limited sampling of the unmixing space by a dataset) can be subject to non-uniqueness, user subjectivity, and in the most serious cases, to selection of physically unrealistic EMs.

In this paper, we develop an improved algorithm for FORC-PCA that addresses these issues. We present a practical implementation that allows the FORC distribution and the FORCs themselves to be reconstructed simultaneously, and describe objective criteria that can be used to guide the most appropriate EM choice to enable quantitative unmixing of FORC diagrams. These improvements to the FORC-PCA method are implemented and integrated into a new version of the FORCem package within FORCinel (Harrison & Feinberg, 2008; Lascu et al., 2015), as described in the supplemental material.

2. Materials and Methods

Three synthetic binary mixtures that contain known proportions of SD, V, and MD magnetite were studied using FORC-PCA. Binary mixtures of SD-V and SD-MD particles were kindly provided by Bruce Moskowitz of the Institute for Rock Magnetism. These samples have been used in several previous studies of magnetic unmixing (Carter-Stiglitz et al., 2001; Dunlop & Carter-Stiglitz, 2006; Lascu et al., 2010). The SD EM is a freeze-dried sample of a cultivated strain of the MV1 magnetotactic bacterium. The magnetosomes have a well-constrained grain-size distribution, with particle sizes of 35x35x53 nm aligned in chains of 10-20 crystals (Moskowitz et

al., 1993). Both the V and MD EMs are synthetic magnetites produced by Wright Industries, with typical grain-size distributions of 1-3 μm and 8-40 μm, respectively (Carvallo & Muxworthy, 2006). The SD-V and SD-MD mixtures were produced by first dispersing the coarser EM in CaF_2 to 0.1% by weight and then adding MV1 to obtain the desired mass proportions. The V-MD mixture was created by weighing the mass of EMs, and dispersing them to a 1% concentration in a fine-grained sucrose matrix. Samples were mixed gently, placed into gelatin capsules and packed with quartz wool or Kimwipe tissues to prevent vibration of the sample during measurement. The mixing proportions of all samples are listed in Table 1. Bulk hysteresis parameters (newly measured for this study) for all samples are listed in Table 2.

Measurements were made at the University of Cambridge on a Lakeshore PMC MicroMag vibrating sample magnetometer. For each sample 174 FORCs were acquired in 1.5 mT field increments with 200 ms averaging time. The FORC data were imported into FORCinel (Harrison & Feinberg, 2008) and processed using the VARIFORC smoothing algorithm (Egli, 2013), resampled on a 2 mT grid, and subjected to PCA analysis following the protocol described by Lascu et al. (2015). EMs were selected from known pure samples to constrain the mixing space. In each case the finest magnetic component was chosen as EM1. The synthetic binary mixtures were then unmixed using PCA and the mixing proportions were calculated.

3. Results

Representative FORC diagrams for each set of studied binary mixtures are shown in Figs. 1-3. The MD EM (Figs. 1a, 3c) has a typical MD FORC diagram dominated by a low-coercivity, vertically spread signal and a weak, high-coercivity, horizontally spread tail, likely related to strong pinning of domain walls by stress fields on surfaces and at internal defects/dislocations (Pike et al., 2001a; Lindquist et al., 2015). The SD EM (Figs. 1c, 2c) has a typical SD FORC diagram for non-interacting uniaxial SD particles, comprising an intense horizontal ridge and a corresponding weak

128 negative signal located close to the negative B_u axis (Muxworthy et al., 2004; Newell, 2005; Egli et
129 al., 2010). The coercivity distribution for the cultured MV1 bacteria is particularly narrow. Some
130 vertical spreading of the horizontal ridge is evident, which indicates either the presence of magnetic
131 interactions among the magnetosome chains, or a small degree of chain collapse (Li et al., 2012;
132 Egli & Winklhofer, 2014; Harrison & Lascu, 2014). A slight vertical offset of the horizontal ridge is
133 likely a viscous magnetization effect caused by the time asymmetry of the FORC measurement
134 protocol (Egli, 2013). The V EM (Figs. 2a, 3a) consists of an intense, closed-contour peak with
135 broad vertical and horizontal spreading, and three weaker, less prominent lobes. Although such
136 FORC signatures can be created by strongly interacting SD clusters (e.g., Carvallo et al., 2005), this
137 explanation can be ruled out here because the known grain size of the sample (1-3 μm) far exceeds
138 the upper SD threshold size. Instead, the broad central peak and three lobes are interpreted as MV
139 and SV processes, respectively, dominated by intra-particle, rather than inter-particle, interactions.
140 A weak negative signal close to the negative B_u axis is visible in Fig. 3a. For V-MD mixtures, the
141 maximum intensity of the FORC signal in each EM is comparable, so that both signals are clearly
142 evident in a ~50:50 mixture (Fig. 3b). The intense positive signal associated with the SD EM,
143 however, dominates the FORC signal of the SD-MD and SD-V mixtures (Fig. 1b, 2b), so that only
144 when >80% of the mixture is constituted by the MD or V EMs does their presence become obvious
145 in the FORC diagram.
146
147 Results of FORC-PCA analysis using the method of Lascu et al. (2015) are shown in Fig. 4. There
148 is a systematic non-linear deviation in all three mixtures between the FORC-PCA calculated (EM1)
149 and actual weight fractions (EM1*) of EMs used to prepare the samples. With EM1 defined to be
150 the finer-grained EM, all three binary mixtures have a concave down relationship between the
151 calculated versus actual mixing proportions. The non-linearity is most pronounced for the SD-MD
152 binary mixture, and is least pronounced for the SD-V binary mixture.
153

4. Origin of the unmixing discrepancy

The difference between mixing proportions derived by FORC-PCA and the known mass proportions of EMs in the synthetic mixtures (Fig. 4) can be explained by the fact that the SD, V, and MD states have different ratios of irreversible to reversible magnetization. The FORC distribution, ρ, is defined as:

$$\rho = -\frac{1}{2}\frac{\partial^2 M}{\partial B_a \partial B_b}, \quad (1)$$

where M is the magnetization, B_a is the reversal field and B_b is the measurement field. Prior to FORC-PCA analysis, each FORC diagram is normalized by its integral:

$$\int\int \rho dB_a dB_b = M_s - M_{rev} = M_{irr}, \quad (2)$$

where M_s is the saturation magnetization, M_{rev} is the reversible component, and M_{irr} is the irreversible component (Pike, 2003). FORC-PCA describes each normalized FORC diagram as the linear sum of normalized EMs, so that the mixing proportions are defined as (e.g., for a binary mixture):

$$\text{EM1} = \frac{m_1 M_{s1} f_1}{M_{irr}}, \text{ and} \quad (3)$$

$$\text{EM2} = 1 - \text{EM1} = \frac{m_2 M_{s2} f_2}{M_{irr}}, \quad (4)$$

where m_1 and m_2 are the mass of each EM, M_{s1} and M_{s2} are the mass-normalized saturation magnetization of each EM, and f_1 and f_2 are the ratio of the irreversible magnetization to saturation magnetization for each EM. The mass proportions of the EMs in the mixture are given by:

$$EM1^* = \frac{m_1}{m_1+m_2}. \quad (5)$$

Rearranging equations 3 and 4 and substituting in 5, we obtain:

$$EM1^* = \frac{EM1}{EM1+f(1-EM1)}, \quad (6)$$

where

$$f = \frac{M_{s1}f_1}{M_{s2}f_2}. \quad (7)$$

The *f* factor expresses how different the EMs are in terms of their irreversible/reversible magnetization contributions. A value of $f = 1$ corresponds to ideal behavior (EM* = EM1), and is obtained only when the EMs contain identical minerals ($M_{s1} = M_{s2}$) with equal ratios of irreversible to saturation magnetization ($f_1 = f_2$). Least-squares fits to plots of EM1 vs EM1* are shown as solid lines in Fig. 4, yielding *f* values of 2.72, 1.52, and 2.69 for the SD-MD, SD-V, and V-MD mixtures, respectively. All EMs contain magnetite; therefore, the different *f* factors indicate that the irreversible contribution to the magnetization of each domain state is different, with SD > V > MD. Although, in principle, equation 6 allows the FORC-PCA proportions to be corrected, prior knowledge of the *f* factor is required. This is not a practical solution when the properties of the EMs are unknown.

5. An improved FORC-PCA algorithm

The non-linear unmixing discrepancy documented above can be corrected by applying PCA to the FORC magnetization surface (which contains both reversible and irreversible contributions), rather than to the FORC distribution (which contains only irreversible contributions); the FORC magnetization surface has been shown previously to mix linearly (Muxworthy et al., 2005). This

206 approach, however, poses a challenge to interactive exploration of the unmixing space that is
207 necessary to identify suitable EMs: as each point in the mixing space is explored, it becomes
208 necessary to estimate ρ over the reconstructed magnetization surface to obtain the corresponding
209 FORC diagram. Here we overcome this problem by applying PCA to the set of six polynomial
210 coefficients that are used to fit the magnetization surface during smoothing of the input FORC
211 diagrams (Pike et al., 1999). In this way, the reconstructed set of coefficients at any given point in
212 the unmixing space can be used to calculate both the magnetization surface and its derivatives
213 simultaneously.
214
215 Our procedure is described as follows. Raw FORC data for a set of samples to be analyzed are
216 imported into FORCinel. A linear high-field slope correction is applied, and a record is kept of the
217 mass normalized M_s value for each sample, for future reference. Here, the slope correction was
218 performed by fitting a straight line to the high-field portion of the FORCs. In cases where the
219 FORCs have not been measured to sufficiently high fields to fully saturate the ferrimagnetic
220 component, it may be desirable to perform the correction using a separately determined value of the
221 high-field susceptibility. The FORCs are normalized to $M_s = 1$, the lower branch subtracted
222 (optionally), and processed using the VARIFORC variable smoothing algorithm (Egli, 2013). For
223 consistency with the published code (see supplementary materials) we use the VARIFORC
224 coordinate scheme (B_c, B_u) rather than the measurement coordinate scheme (B_a, B_b) in the
225 following. For each output point in a processed FORC diagram, a weighted second-order
226 polynomial fit is performed to the local magnetization surface over a rectangular area defined by the
227 horizontal and vertical smoothing factors (Egli, 2013):
228
229 $$M(B_c, B_u) = a_0 + a_1 B_c + a_2 B_u + a_3 B_c^2 + a_4 B_c B_u + a_5 B_u^2 \quad . \quad (8)$$
230
231 The FORC distribution (eqn. 1) is then given by:

$$\rho = \frac{a_3 - a_5}{4}. \quad (9)$$

In order to analyze sets of FORC diagrams that may have been acquired using different measurement protocols, each polynomial coefficient in eqn. 8 is interpolated bi-linearly onto a rectangular grid, capturing a specified region of interest. For a rectangular grid containing N points, there will be $6N$ observations for each FORC diagram, corresponding to the six bi-linearly interpolated polynomial coefficients for each point. The FORC-PCA method of Lascu et al. (2015) is then applied, simply replacing the N values of the FORC distribution with the $6N$ polynomial coefficients for each sample. Once the number of significant PCs has been chosen ($n \leq 3$, corresponding to a maximum of 4 EMs), low-rank approximations of both the magnetization surface and the FORC distribution can be reconstructed for any chosen location within the resulting unmixing space (score plot). Exploring the unmixing space to identify potential EMs can now be performed interactively, guided by both the reconstructed magnetization and corresponding FORC diagram.

A complication occurs when the option to subtract the lower branch from the normalized FORCs prior to smoothing is chosen. Lower-branch subtraction was introduced by Egli (2013) to improve smoothing performance in the vicinity of the $B_b = 0$ axis (an axis extending from the origin at a -45° angle in VARIFORC coordinate space). Lower-branch subtraction reduces significantly the appearance of smoothing artefacts along this axis when using variable smoothing protocols because it removes sigmoidal magnetization contributions that are poorly described by a second-order polynomial. When smoothing is performed after lower-branch subtraction, the set of polynomial coefficients in eqn. 8 describes the subtracted magnetization surface rather than the desired full magnetization surface. In order to reconstruct the full magnetization surface, a second smoothing step is performed on a synthetic 2D magnetization surface created using just the lower-branch

signal. This lower-branch surface is fitted using eqn. 8, but with the strict constraint that $a_3 = a_5$, thereby ensuring that the FORC distribution (and its associated artefacts) associated with the lower-branch surface is zero (eqn. 9). Polynomial coefficients resulting from the fit to the lower-branch surface are then added to those resulting from the fit to the lower-branch subtracted magnetization surface, which are then used as input to the FORC-PCA. This double-smoothing procedure allows the full magnetization surface to be reconstructed from the chosen PC combination, while retaining an artefact-free representation of the reconstructed FORC diagram.

Heslop & Roberts (2012a) demonstrated that, because of the corrupting effects of measurement noise, it is necessary to calculate statistical significance levels to identify the parts of a FORC distribution where ρ is significantly above the signal-to-noise ratio. Use of PCA to provide a low-rank approximation of a collection of measured FORC diagrams is also an effective approach to reduce the influence of noise in representing a mixing system (Heslop, 2015). Therefore, while PCA will not eliminate noise completely, its effect on the representation of the mixing system and on the identified EMs is reduced substantially compared to individual FORC diagrams.

Results of the new algorithm applied to the synthetic binary mixtures are shown in Figs. 5-7. The V-MD mixture (Fig. 5) is well described as a binary mixture, with 99% of the variance in the dataset explained by PC1. Pure EMs are included within the dataset, which leads to no ambiguity in the choice of EM1 (V) and EM2 (MD) (Fig. 5a, b). The SD-MD mixture (Fig. 6) can be approximated as a binary mixture, with 95% of the variance being explained by the first principal component (PC1). However, a small but significant second principal component (PC2) is needed to bring the variance explained to >99% (Fig. 6g). Without including PC2, it is not possible to isolate completely a pure MD EM. This effect is caused by subtle coercivity differences of the MV1 bacteria from sample to sample, which only become apparent because of the intense and narrow nature of their FORC distribution. Possible explanations for the coercivity difference between

284 samples include differences in oxidation state that resulted from sample storage in air for over 10
285 years, or different degrees of bacterial chain collapse. By including PC2, small coercivity
286 differences can be taken into account, enabling a pure MD EM to be identified (EM1, Fig. 6a),
287 along with two SD EMs (EM2 and EM3) that differ only in their average coercivity (Figs. 6b and c;
288 Table 3). Hence, PC1 describes the binary mixing between SD and MD EMs, and PC2 accounts for
289 the varying coercivity of the SD MV1 component. A similar approach was taken to describe the
290 SD-V mixture (Fig. 7), although the coercivity variation of the MV1 samples is less pronounced
291 (99% of the variance is explained by PC1 alone). In all three cases, the mixing proportions derived
292 from FORC-PCA agree well with the known mass fractions. The 2σ differences between calculated
293 and observed proportions are 2%, 5%, and 6% for the SD-MV, SD-V, and MD-V binary mixtures,
294 respectively. These observations provide an empirical estimate of the error in the unmixing
295 proportions that is likely to be achieved using FORC-PCA in optimal cases (i.e., where the mixing
296 space is well sampled by the dataset).
297
298 **6. Feasibility metrics**
299 An inherent part of the FORC-PCA method is the supervised exploration of the unmixing
300 space in order to identify appropriate EMs (Lascu et al., 2015). This process is only unambiguous
301 when the sample set includes examples of each EM that is being solved for (as is approximately the
302 case for the binary mixtures studied here). When the sampling of the unmixing space in incomplete,
303 however, the method relies heavily on the expertise of the user to identify (a) EMs that enclose the
304 entire set of sample scores (with the exception of outliers identified by residual analysis), (b) pure
305 EMs (i.e., that do not contain any residual contributions from the other EMs), and (c) EMs that are
306 physically realistic (i.e., the reconstructed FORC diagram for each EM corresponds to an achievable
307 FORC geometry based on knowledge of the magnetic mineralogy and the responses that can be
308 modelled physically) (Harrison & Lascu, 2014). With access to only the reconstructed FORC
309 diagram, identification of physically unrealistic regions of the unmixing space relies on subjective

criteria. The availability of reconstructed FORCs, however, provides objective information from which criteria can be defined to assess the physical feasibility of the corresponding FORC diagram. Following the approach of Heslop & Roberts (2012b), three criteria that can be applied to assess the feasibility of reconstructed FORCs are: (a) saturation (i.e., no FORC should exceed the normalized value of $M_s = 1$), (b) monotonicity (i.e., the first derivative of a FORC with respect to the measurement field should remain nonnegative), and (c) crossing (i.e., the first derivative of the magnetization surface with respect to the reversal field should remain positive, meaning that FORCs do not intersect each other). Each of these metrics can be used on their own, or in combination, to define the region of unmixing space that is physically realistic. The EMs should be contained entirely within that region.

We define three metrics for each of the feasibility criteria, which vary from 0 (completely unsatisfied) to 1 (completely satisfied):

$$m_{saturation} = \frac{\sum |M_A|}{\sum |M|}, \tag{10}$$

where M_A is the subset of the magnetization, M, that satisfies the condition $|M| \leq 1$;

$$m_{monotonicity} = \frac{\sum \left(\frac{dM}{dB_a}\right)_A}{\sum \left|\frac{dM}{dB_a}\right|}, \tag{11}$$

where $\left(\frac{dM}{dB_a}\right)_A$ is the subset of $\frac{dM}{dB_a}$ that satisfies the condition $\frac{dM}{dB_a} \geq 0$; and

$$m_{crossing} = \frac{\sum \left(\frac{dM}{dB_b}\right)_A}{\sum \left|\frac{dM}{dB_b}\right|}, \tag{12}$$

where $\left(\frac{dM}{dB_b}\right)_A$ is the subset of $\frac{dM}{dB_b}$ that satisfies the condition $\frac{dM}{dB_b} \geq 0$.

The metrics can be combined into a single feasibility metric, *m*, by multiplying them together in any combination. By calculating *m* over a grid of points, contours of feasibility can be used to indicate the region of unmixing space where the criteria are satisfied fully ($m = 1$). In practice, some allowance is needed for the fact that we are dealing with a low-rank approximation to the data, that some non-monotonicity may be genuinely present (e.g., for SP grains), and that experimental noise can cause FORCs to cross as saturation is approached. This means that *m* values slightly less than 1 should be allowable. Here we take $m > 0.99$ as a reasonable (although arbitrary) guideline of acceptability (Fig. 6g and 7g). Given the essentially binary nature of the mixtures, the placement of EM3 slightly outside the $m = 0.99$ contour in Figs. 6g and 7g has been done to maintain EM2 and EM3 at a constant value of PC1 away from EM1, whilst ensuring that all data points are contained within the mixing triangle.

A fourth metric, which should be used independently of the other three, describes the amount of negative signal in the processed FORC diagram. Given that negative regions are an intrinsic feature of many FORC diagrams, this metric is less stringent than the others (values significantly < 1 are acceptable). However, there are specific domain states that do not have intrinsically negative regions, or have only weakly negative regions, so evaluating this metric can be helpful to define the location of specific EMs. For example, inappropriate appearance of strong negative signals can be caused by over-subtraction of other EMs, which provides a good indication that EM selection has strayed too far from the data. The positivity metric is defined as:

$$m_{positivity} = \frac{\sum|\rho_A|}{\sum|\rho|}, \quad (13)$$

where ρ_A is the subset of the FORC distribution, ρ, that satisfies the conditions $\rho \geq 0$. Steep drops in $m_{\text{positivity}}$ may indicate that over-subtraction of other EMs is occurring.

7. Example

To illustrate the new FORC-PCA algorithm applied to natural mixtures of different domain states, we analyzed a suite of greigite-bearing clays from Florindo et al. (2007), which were deposited between 800 ka and 600 ka in the Tiber River coastal alluvial plain around Rome. A total of 17 FORCs were measured, 14 of which contain magnetostatically interacting SD greigite mixed with varying amounts of a SP/SD greigite. The other 3 samples contain the SP/SD signal only. The latter samples were significantly less magnetic than the former, and have noisy processed FORC diagrams. FORC data from these three samples were averaged to produce a single representative example of the pure SP/SD component. This averaged FORC and the other 14 FORCs were then analyzed using FORC-PCA (Fig. 8). Only two PCs are needed to explain over 90% of the variance in the dataset, with a third PC bringing the variance explained to 98%. For illustrative purposes, we use a two-PC model constructed from PC1 and PC3, which provides the most convenient projection of the key mixing trends. Three EMs are identified. Key features of EM1 (Fig. 8a) are a negative region close to the negative B_u axis (1), a second negative region that is elongated and steeply angled down and to the right (2), and a kidney-shaped positive peak that is strongly offset in the negative B_u direction and extends only slightly above the $B_u = 0$ axis (3). All three of these features are diagnostic of relatively weakly interacting SD greigite grains (Roberts et al., 2011) with cubic magnetocrystalline anisotropy (Harrison & Lascu, 2014). Key features of EM2 (Fig. 8b) are a negative region close to the negative B_u axis (1) and a rounded positive peak that is offset in the negative B_u direction and extends far above the $B_u = 0$ axis (2). Both features are diagnostic of strongly interacting SD greigite (Roberts et al., 2011; Harrison & Lascu, 2014). Key features of EM3 (Fig. 8c) are a low-coercivity ridge with maximum intensity at 0 mT (1) and an increasing positive signal extending along the negative B_u axis (2). Feature 1 is characteristic of non-

385 interacting SD greigite particles with coercivities that have been reduced by thermal activation
386 (Pike et al., 2001b; Rowan & Roberts, 2006). Feature 2 is likely due to viscous SP behavior, which
387 leads to the negative initial slope of each FORC (arrow in Fig. 8f; Pike et al., 2001b). However,
388 given that the intensity of this feature continues to increase, even as reverse saturation is
389 approached, it is also likely to be partially an instrumental artefact.
390
391 The choice of EMs in this case has been guided by the following principles. First, EM3 is fixed by
392 inclusion of the pure SP/SD EM in the dataset. This sample plots to the far right of the unmixing
393 space (Fig. 8g), close to but within the guideline boundary of physical feasibility. Moving left, away
394 from EM3 in a direction parallel to the PC1 axis (which describes the largest mode of variability in
395 the dataset), yields a binary mixture of EM3 and a moderately-interacting SD greigite EM (EM1).
396 The most extreme left-hand data point lies close to the guideline boundary of physical feasibility.
397 However, the FORC diagram for this data point contains a trace residual of EM3. In order to obtain
398 a pure EM, one must move further to the left. The guideline boundary of physical feasibility places
399 a limit on how far to the left one can go before the reconstructed FORCs for EM1 become
400 physically unrealistic. We place EM1 at the $m = 0.99$ threshold, which yields a physically realistic
401 pure EM with no residual trace of EM3. The placement of EM2 is more difficult because it lies well
402 within the guideline region of physical feasibility. Here, the positivity index (eqn. 13) provides an
403 additional guideline (inset to Fig. 8g). A steep drop in $m_{\text{positivity}}$ is observed if EM2 is placed too far
404 along the positive PC2 axis, which is caused by over-subtraction of EM1 from the reconstructed
405 FORC diagram. If EM2 is placed too far along the positive PC1 axis then not all the data are
406 enclosed by the unmixing space. Combined, these two principles place important constraints on the
407 location of EM2, and produce a reconstructed FORC diagram with a recognizable geometry and
408 minimal residual traces of EM1 and EM3.
409

Having defined the unmixing space, the proportions of the three EMs can be determined (Fig. 8h). Two distinct mixing trends can be identified in the data: a mixing between SP/SD and strongly interacting SD greigite, and one between weakly and strongly interacting SD greigite. The first mixing trend can be explained by grain growth of authigenic greigite from small, non-interacting particles below the SP threshold size to larger, stable SD particles in closely packed clusters within framboids with strong interactions (Rowan & Roberts, 2006). The second mixing trend can be explained as a weakening of the interactions between SD greigite particles, driven by a lowering of the packing fraction. A possible mechanism to explain this trend is the progressive replacement of strongly interacting greigite framboids by thermodynamically stable, paramagnetic pyrite. This process was recently identified by Ebert et al. (2018) using high-resolution magnetic force microscopy imaging. This interpretation is consistent with the lack of a mixing trend between EM1 (SP/SD) and EM3 (weakly interacting SD), which cannot be achieved in this pyrite replacement scenario without first going through the strongly interacting SD greigite EM.

8. Discussion

Unmixing the magnetic properties of rocks, sediments, and soils is a primary task in rock magnetism. Numerous methods exist to tackle this problem (e.g., Robertson & France, 1994; Kruiver et al., 2001; Dunlop, 2002a, 2002b; Egli, 2004a, 2004b, 2004c; Franke et al. 2007; Heslop & Dillon, 2007; Lascu et al., 2010, 2015; Ludwig et al., 2013; Lagroix & Guyodo, 2017) as well as an extensive toolbox of magnetic proxies that are designed to highlight specific magnetic mineralogy variations in environmental contexts (Evans & Heller, 2003; Liu et al., 2012). No single method is perfect for all cases, and usually a combination of methods is needed to unmix all magnetic components contained within a material. In particular, preparatory studies performed at high sampling resolution provide an efficient way to prescreen a dataset, and to identify samples that are closest to potential EMs (e.g., EM3 in Fig. 8). The FORC-PCA method is ideally suited to characterizing ferrimagnetic minerals, with an emphasis on discriminating populations of grains that

differ in domain state, coercivity distribution, anisotropy, and interaction field (i.e., aspects to which FORC diagrams are particularly sensitive). Here we have resolved many of the outstanding issues associated with the original FORC-PCA method of Lascu et al. (2015), including solution of the linear mixing equation, the ability to identify SP EMs that are dominated by reversible magnetizations, and reducing ambiguities in defining the unmixing space. Excellent agreement between our calculated proportions for SD-MV and SD-V mixtures contrasts starkly with attempts to unmix these samples using either linear or non-linear mixing in a Day plot (Day et al., 1977; Dunlop & Carter-Stiglitz, 2006). Failure of the Day plot unmixing approach was explained by Dunlop & Carter-Stiglitz (2006) as due to the squareness of hysteresis loops for MV1 bacteria, which violates the linear assumption of the unmixing model (Dunlop, 2002a, 2002b). This illustrates one of the key advantages of PCA, which makes no prior assumptions about the shape of the EM signals (Heslop, 2015).

The need to use three EMs to describe binary SD-V and SD-MD mixtures highlights an important underlying assumption of the FORC-PCA method, namely that the properties of each EM are constant throughout a sample set, with only the mixing proportions varying from sample to sample. Whenever this assumption is not met, additional 'fictive' EMs may be needed to define adequately the total variability within a dataset. This is clearly the case for the MV1-bearing mixtures, where significant coercivity variations of the bacterial component exist from sample to sample. Given the narrow coercivity distribution of the MV1 bacteria, use of a third EM becomes necessary to isolate a pure V or MD EM. Most natural samples have broader coercivity distributions, however, and as long as intra-EM variability is low compared to inter-EM variability, 'fictive' EMs are not typically necessary. The likelihood that 'fictive' EMs will be needed to account for intra-EM variability increases as the size of the FORC dataset increases. For large datasets, it may be necessary to perform a series of FORC-PCA analyses on subsets of the data. This approach allows commonalities between EMs extracted from different subsets to be identified, and the nature of

intra-EM variability to be explored. In other cases (e.g., grain-size sorting of a detrital component), sample-to-sample variability is physically linked to a single EM with continuously variable properties, rather than to a mechanical mixture of EMs with fixed properties. In these cases, FORC-PCA generates two or more 'fictive' EMs that recreate inter-sample variations, but do not correspond to fixed physical components of the system. Nevertheless, the mixing proportions of 'fictive' EMs provide a useful co-ordinate system with which to quantify the extent of inter-sample variation, and may be used to identify variation trends and clusters of behavior.

The ability to unmix up to four[1] EMs, each with their own distinct domain state, coercivity and interaction field distribution, takes us beyond the routine characterization that is commonly considered 'good enough' for most paleomagnetic studies, and largely addresses the ambiguities (Roberts et al., 2018) involved in interpreting the widely used Day diagram (Day et al., 1977). The new algorithm provides a full set of FORCs for each EM, which allows additional hysteresis properties to be derived for each EM. In some cases, this additional information can be used to check for consistency with the interpreted physical origin of each EM (e.g., if the FORC diagram of the EM suggests non-interacting, uniaxial SD behavior, then M_r/M_s values close to 0.5 and B_{cr}/B_c values close to 1 would be expected). Compared to a Day diagram, hysteresis ratios of extracted EMs acquire enhanced physical meaning because the effects of mixing have been deconvolved. The use of feasibility metrics reduces (but does not eliminate) the ambiguity involved in defining EMs when the unmixing space is sampled incompletely. This development should help to make the FORC-PCA method accessible to a wider audience. However, it should always be borne in mind that feasibility metrics are only a guideline – good choices, as ever, rely on the expertise and judgement of the user.

9. Conclusions

[1] There is no limit on the number of EMs that can be mathematically defined. However, beyond four EMs, visualization and interactive exploration of the unmixing space becomes impractical.

1. Our improved FORC-PCA algorithm addresses many of the outstanding issues with the initial method of Lascu et al. (2015), including solving the linear mixing problem and providing the ability to characterize SP EMs that are dominated by reversible magnetizations.
2. The new method enables both the reconstructed FORC magnetization surface and the corresponding FORC diagram of each EM to be identified.
3. Access to the reconstructed FORC magnetization surface enables objective criteria to be defined that guide the choice of physically realistic EMs. A mixture of robust criteria (e.g., saturation, monotonicity, and crossing) and more flexible criteria (e.g., positivity) can be used to help reduce the subjectivity of defining the unmixing space.
4. The method has been applied successfully to quantify synthetic binary mixtures with EMs with contrasting domain states, and to aid interpretation of diagenetic trends in greigite-bearing sedimentary environments.
5. The improved FORC-PCA algorithm provides a powerful method to discriminate between populations of grains with different domain state, coercivity distribution, anisotropy type, and interaction field distribution. The increased value of the information that this analysis yields far outweighs the additional measurement time that is needed, providing a way to take routine rock magnetic characterization far beyond the ambiguities of the widely used Day diagram.

Acknowledgements

We thank Andrew Newell and Ramon Egli for their helpful and constructive reviews of the manuscript. This work was supported financially by the Australian Research Council through grant DP160100805 and by the European Research Council under the European Union's Seventh Framework Programme (FP/2007–2013)/ERC grant agreement number 320750. Samples of SD-V and SD-MV mixtures were kindly provided by Bruce Moskowitz of the Institute for Rock Magnetism, University of Minnesota. All data used in this study is available for download as part of the online supporting information.

513

514 **References**

515 Carter-Stiglitz, B., Moskowitz, B., & Jackson, M. (2001). Unmixing magnetic assemblages and the
516 magnetic behavior of bimodal mixtures. *Journal of Geophysical Research: Solid Earth*,
517 *106*(B11), 26397. https://doi.org/10.1029/2001JB000417

518 Carvallo, C., & Muxworthy, A. (2006). Low-temperature first-order reversal curve (FORC)
519 diagrams for synthetic and natural samples. *Geochemistry, Geophysics, Geosystems*, *7*(9),
520 Q09003. https://doi.org/10.1029/2006GC001299

521 Carvallo, C., Dunlop, D., & Ozdemir, O. (2005). Experimental comparison of FORC and remanent
522 Preisach diagrams. *Geophysical Journal International*, *162*(3), 747–754. Retrieved from
523 papers://2973f1d5-d696-469c-80fa-0e7ffe9241d4/Paper/p421

524 Channell, J. E. T., Harrison, R. J., Lascu, I., McCave, I. N., Hibbert, F. D., & Austin, W. E. N.
525 (2016). Magnetic record of deglaciation using FORC-PCA, sortable-silt grain size, and
526 magnetic excursion at 26 ka, from the Rockall Trough (NE Atlantic). *Geochemistry,*
527 *Geophysics, Geosystems*, *17*(5), 1823–1841. https://doi.org/10.1002/2016GC006300

528 Day, R., Fuller, M., & Schmidt, V. A. (1977). Hysteresis properties of titanomagnetites: grain-size
529 and compositional dependence. *Physics of the Earth and Planetary Interiors*, *13*, 260–267.

530 Donnelly, C., Guizar-Sicairos, M., Scagnoli, V., Gliga, S., Holler, M., Raabe, J., & Heyderman, L.
531 J. (2017). Three-dimensional magnetization structures revealed with X-ray vector
532 nanotomography. *Nature*, *547*(7663), 328–331. https://doi.org/10.1038/nature23006

533 Dunlop, D. J. (2002a). Theory and application of the Day plot (Mrs/Ms versus Hcr/Hc) 1.
534 Theoretical curves and tests using titanomagnetite data. *Journal of Geophysical Research:*
535 *Solid Earth*, *107*(B3), 2056. https://doi.org/10.1029/2001JB000486

536 Dunlop, D. J. (2002b). Theory and application of the Day plot (Mrs/Ms versus Hcr/Hc) 2.
537 Application to data for rocks, sediments, and soils. *Journal of Geophysical Research: Solid*
538 *Earth*, *107*(B3), 2057. https://doi.org/10.1029/2001JB000487

539 Dunlop, D. J., & Carter-Stiglitz, B. (2006). Day plots of mixtures of superparamagnetic, single-
540 domain, pseudosingle-domain, and multidomain magnetites. *Journal of Geophysical Research:*
541 *Solid Earth*, *111*(B12), B12S09. https://doi.org/10.1029/2006JB004499
542 Ebert, Y., Shaar, R., Emmanuel, S., Nowaczyk, N., & Stein, M. (2018). Overwriting of sedimentary
543 magnetism by bacterially mediated mineral alteration. *Geology*, *46*(4), 2–5.
544 https://doi.org/https://doi.org/10.1130/G39706.1
545 Egli, R. (2004a). Characterization of Individual Rock Magnetic Components by Analysis of
546 Remanence Curves, 1. Unmixing Natural Sediments. *Studia Geophysica et Geodaetica*, *48*(2),
547 391–446. https://doi.org/10.1023/B:SGEG.0000020839.45304.6d
548 Egli, R. (2004b). Characterization of individual rock magnetic components by analysis of
549 remanence curves. *Physics and Chemistry of the Earth*, *29*(13–14), 851–867.
550 https://doi.org/10.1016/j.pce.2004.04.001
551 Egli, R. (2004c). Characterization of individual rock magnetic components by analysis of
552 remanence curves. 3. Bacterial magnetite and natural processes in lakes. *Physics and*
553 *Chemistry of the Earth*, *29*(13–14), 869–884. https://doi.org/10.1016/j.pce.2004.03.010
554 Egli, R. (2006). Theoretical aspects of dipolar interactions and their appearance in first-order
555 reversal curves of thermally activated single-domain particles. *Journal of Geophysical*
556 *Research: Solid Earth*, *111*(B12), B12S17. https://doi.org/10.1029/2006JB004567
557 Egli, R. (2013). VARIFORC: An optimized protocol for calculating non-regular first-order reversal
558 curve (FORC) diagrams. *Global and Planetary Change*, *110*, 302–320.
559 https://doi.org/10.1016/j.gloplacha.2013.08.003
560 Egli, R., Chen, A. P., Winklhofer, M., Kodama, K. P., & Horng, C.-S. (2010). Detection of
561 noninteracting single domain particles using first-order reversal curve diagrams. *Geochemistry,*
562 *Geophysics, Geosystems*, *11*(1), Q01Z11. https://doi.org/10.1029/2009GC002916
563 Egli, R., & Winklhofer, M. (2014). Recent developments on processing and interpretation aspects
564 of first-order reversal curves (FORC). *Proc. Kazan. Univ.*, *156*(January), 14–53.

565 Evans, M. E., & Heller, F. (2003). *Environmental magnetism principles and applications of*
566 *enviromagnetics*. Academic Press, Amsterdam.
567 Florindo, F., Karner, D., Marra, F., Renne, P. R., Roberts, A. P., & Weaver, R. (2007).
568 Radioisotopic age constraints for Glacial Terminations IX and VII from aggradational sections
569 of the Tiber River delta in Rome, Italy. *Earth and Planetary Science Letters*, *256*(1–2), 61–80.
570 https://doi.org/10.1016/j.epsl.2007.01.014
571 Franke, C., Frederichs, T., & Dekkers, M. J. (2007). Efficiency of heavy liquid separation to
572 concentrate magnetic particles. *Geophysical Journal International*, *170*(3), 1053–1066.
573 https://doi.org/10.1111/j.1365-246X.2007.03489.x
574 Harrison, R. J., & Feinberg, J. M. (2008). FORCinel: An improved algorithm for calculating first-
575 order reversal curve distributions using locally weighted regression smoothing. *Geochemistry,*
576 *Geophysics, Geosystems*, *9*(5), Q05016. https://doi.org/10.1029/2008GC001987
577 Harrison, R. J., & Lascu, I. (2014). FORCulator: A micromagnetic tool for simulating first-order
578 reversal curve diagrams. *Geochemistry, Geophysics, Geosystems*, *15*(12), 4671–4691.
579 https://doi.org/10.1002/2014GC005582
580 Heslop, D. (2015). Numerical strategies for magnetic mineral unmixing. *Earth-Science Reviews*,
581 *150*, 256–284. https://doi.org/10.1016/j.earscirev.2015.07.007
582 Heslop, D., Roberts, A. P., & Chang, L. (2014). Characterizing magnetofossils from first-order
583 reversal curve (FORC) central ridge signatures. *Geochemistry, Geophysics, Geosystems*, *15*(6),
584 2170–2179. https://doi.org/10.1002/2014GC005291
585 Heslop, D., & Dillon, M. (2007). Unmixing magnetic remanence curves without a priori
586 knowledge. *Geophysical Journal International*, *170*(2), 556–566.
587 https://doi.org/10.1111/j.1365-246X.2007.03432.x
588 Heslop, D., & Roberts, A. P. (2012a). Estimation of significance levels and confidence intervals for
589 first-order reversal curve distributions. *Geochemistry Geophysics Geosystems*, *13*(12),
590 Q12Z40. https://doi.org/10.1029/2012GC004115

591 Heslop, D., & Roberts, A. P. (2012b). A method for unmixing magnetic hysteresis loops. *Journal of*
592 *Geophysical Research: Solid Earth*, *117*(B3), B03103. https://doi.org/10.1029/2011JB008859
593 Jolliffe, I. T. (2002) Principal Component Analysis. Springer-Verlag, New York, pp. 488.
594 Kruiver, P. P., Dekkers, M. J., & Heslop, D. (2001). Quantification of magnetic coercivity
595 components by the analysis of acquisition curves of isothermal remanent magnetisation. *Earth*
596 *and Planetary Science Letters*, *189*(3–4), 269–276. https://doi.org/10.1016/S0012-
597 821X(01)00367-3
598 Lagroix, F., & Guyodo, Y. (2017). A new tool for separating the magnetic mineralogy of complex
599 mineral assemblages from low temperature magnetic behavior. *Frontiers in Earth Science*, *5*,
600 1–11. https://doi.org/10.3389/feart.2017.00061
601 Lascu, I., Banerjee, S. K., & Berquó, T. S. (2010). Quantifying the concentration of ferrimagnetic
602 particles in sediments using rock magnetic methods. *Geochemistry, Geophysics, Geosystems*,
603 *11*(8), Q08Z19. https://doi.org/10.1029/2010GC003182
604 Lascu, I., Harrison, R. J., Li, Y., Muraszko, J. R., Channell, J. E. T., Piotrowski, A. M., & Hodell,
605 D. A. (2015). Magnetic unmixing of first-order reversal curve diagrams using principal
606 component analysis. *Geochemistry, Geophysics, Geosystems*, *16*(9), 2900–2915.
607 https://doi.org/10.1002/2015GC005909
608 Li, J., Wu, W., Liu, Q., & Pan, Y. (2012). Magnetic anisotropy, magnetostatic interactions and
609 identification of magnetofossils. *Geochemistry, Geophysics, Geosystems*, *13*(12), Q10Z51.
610 https://doi.org/10.1029/2012GC004384
611 Lindquist, A. K., Feinberg, J. M., Harrison, R. J., Loudon, J. C., & Newell, A. J. (2015). Domain
612 wall pinning and dislocations: Investigating magnetite deformed under conditions analogous to
613 nature using transmission electron microscopy. *Journal of Geophysical Research: Solid Earth*,
614 *120*(3), 1415–1430. https://doi.org/10.1002/2014JB011335
615 Liu, Q., Roberts, A. P., Larrasoaña, J. C., Banerjee, S. K., Guyodo, Y., Tauxe, L., & Oldfield, F.
616 (2012). Environmental magnetism: Principles and applications. *Reviews of Geophysics*, *50*(4),

RG4002. https://doi.org/10.1029/2012RG000393

Ludwig, P., Egli, R., Bishop, S., Chernenko, V., Frederichs, T., Rugel, G., … Orgeira, M. J. (2013). Characterization of primary and secondary magnetite in marine sediment by combining chemical and magnetic unmixing techniques. *Global and Planetary Change*, *110*, 321–339. https://doi.org/10.1016/j.gloplacha.2013.08.018

Maxbauer, D. P., Feinberg, J. M., Fox, D. L., & Nater, E. A. (2017). Response of pedogenic magnetite to changing vegetation in soils developed under uniform climate, topography, and parent material. *Scientific Reports*, *7*(1), 17575. https://doi.org/10.1038/s41598-017-17722-2

Moskowitz, B., Frankel, R. B., & Bazylinski, D. A. (1993). Rock magnetic criteria for the detection of biogenic magnetite. *Earth and Planetary Science Letters*, *120*, 283–300.

Muxworthy, A. R., King, J., & Helsop, D. (2005). Assessing the ability of first-order reversal curve (FORC) diagrams to unravel complex magnetic signals. *Journal of Geophysical Research*, *110*(B1), B01105. https://doi.org/10.1029/2004JB003195

Muxworthy, A., Heslop, D., & Williams, W. (2004). Influence of magnetostatic interactions on first-order-reversal-curve (FORC) diagrams: a micromagnetic approach. *Geophysical Journal International*, *158*(3), 888–897. https://doi.org/10.1111/j.1365-246X.2004.02358.x

Newell, A. J. (2005). A high-precision model of first-order reversal curve (FORC) functions for single-domain ferromagnets with uniaxial anisotropy. *Geochemistry, Geophysics, Geosystems*, *6*(5), Q05010. https://doi.org/10.1029/2004GC000877

Pike, C. R. (2003). First-order reversal-curve diagrams and reversible magnetization. *Physical Review B*, *68*(10), 104424. https://doi.org/10.1103/PhysRevB.68.104424

Pike, C. R., Roberts, A. P., & Verosub, K. L. (1999). Characterizing interactions in fine magnetic particle systems using first order reversal curves. *Journal of Applied Physics*, *85*(9), 6660–6667.

Pike, C., Roberts, A., Dekkers, M., & Verosub, K. (2001a). An investigation of multi-domain hysteresis mechanisms using FORC diagrams. *Physics of the Earth and Planetary Interiors*,

643 *126*, 11–25.
644 Pike, C. R., Roberts, A. P., & Verosub, K. L. (2001b). First-order reversal curve diagrams and
645 thermal relaxation effects in magnetic particles. *Geophysical Journal International*, *145*, 721–
646 730.
647 Plaza-Morlote, M., Rey, D., Santos, J. F., Ribeiro, S., Heslop, D., Bernabeu, A., … Martíns, V.
648 (2017). Southernmost evidence of large European Ice Sheet-derived freshwater discharges
649 during the Heinrich Stadials of the Last Glacial Period (Galician Interior Basin, Northwest
650 Iberian Continental Margin). *Earth and Planetary Science Letters*, *457*, 213–226.
651 https://doi.org/10.1016/j.epsl.2016.10.020
652 Roberts, A., Chang, L., Rowan, C., Horng, C., & Florindo, F. (2011). Magnetic properties of
653 sedimentary greigite (Fe 3S 4): An update. *Reviews of Geophysics*, *49*(1), RG1002.
654 Roberts, A. P., Tauxe, L., Heslop, D., Zhao, X., & Jiang, Z. (2018). A Critical Appraisal of the
655 "Day" Diagram. *Journal of Geophysical Research: Solid Earth*.
656 https://doi.org/10.1002/2017JB015247
657 Roberts, A. P., Heslop, D., Zhao, X., & Pike, C. R. (2014). Understanding fine magnetic particle
658 systems through use of first-order reversal curve diagrams. *Reviews of Geophysics*, *52*(4), 557–
659 602. https://doi.org/10.1002/2014RG000462
660 Roberts, A. P., Pike, C. R., & Verosub, K. L. (2000). First order reversal curve diagrams: A new
661 tool for characterising the magnetic properties of natural samples. *Journal of Geophysical*
662 *Research: Solid Earth*, *105*(B12), 28461–28475.
663 Roberts, A. P., Almeida, T. P., Church, N. S., Harrison, R. J., Heslop, D., Li, Y., … Zhao, X.
664 (2017). Resolving the Origin of Pseudo-Single Domain Magnetic Behavior. *Journal of*
665 *Geophysical Research: Solid Earth*, *122*(12), 9534–9558.
666 https://doi.org/10.1002/2017JB014860
667 Robertson, D. J., & France, D. E. (1994). Discrimination of remanence-carrying minerals in
668 mixtures, using isothermal remanent magnetisation acquisition curves. *Physics of the Earth*

669 *and Planetary Interiors*, *82*(3–4), 223–234. https://doi.org/10.1016/0031-9201(94)90074-4
670 Rowan, C. J., & Roberts, A. P. (2006). Magnetite dissolution, diachronous greigite formation, and
671 secondary magnetizations from pyrite oxidation: Unravelling complex magnetizations in
672 Neogene marine sediments from New Zealand. *Earth and Planetary Science Letters*, *241*,
673 119–137. https://doi.org/10.1016/j.epsl.2005.10.017
674 Zhao, X., Roberts, A. P., Heslop, D., Paterson, G. A., Li, Y., & Li, J. (2017). Magnetic domain state
675 diagnosis using hysteresis reversal curves. *Journal of Geophysical Research: Solid Earth*,
676 *122*(7), 4767–4789. https://doi.org/10.1002/2016JB013683
677 Zhao, X., Heslop, D., & Roberts, A. P. (2015). A protocol for variable-resolution first-order reversal
678 curve measurements. *Geochemistry, Geophysics, Geosystems, 16*(5), 1364–1377.
679 https://doi.org/10.1002/2014GC005680

680

681 **Figure Captions**

682

683 **Figure 1.** Experimental FORC diagrams for SD-MD mixtures. Smoothing performed using FORCinel with
684 VARIFORC parameters S_{c0} = 7, S_{c1} = 7, S_{b0} = 5, S_{b1} = 7, λ_c= 0.1, and λ_b= 0.1. Mixing proportions are (**a**)
685 100%, MD 0% SD, (**b**) 88%, MD 12% SD, and (**c**) 8% MD, 92% SD.

686

687 **Figure 2.** Experimental FORC diagrams for SD-V mixtures. Smoothing performed using FORCinel with
688 VARIFORC parameters S_{c0} = 7, S_{c1} = 12, S_{b0} = 5, S_{b1} = 12, λ_c= 0, and λ_b= 0. Mixing proportions are (**a**)
689 100% V, 0% SD, (**b**) 80% V, 20% SD, and (**c**) 5% V, 95% SD.

690

691 **Figure 3.** Experimental FORC diagrams for V-MD mixtures. Smoothing performed using FORCinel with
692 VARIFORC parameters S_{c0} = 7, S_{c1} = 7, S_{b0} = 5, S_{b1} = 7, λ_c=0.1, and λ_b=0.1. Mixing proportions are (**a**)
693 100% V, 0% MD, (**b**) 49% V, 51% MD, and (**c**) 0% V, 100% MD.

694

695 **Figure 4.** Comparison of mixing proportions derived from FORC-PCA (EM) using the method of Lascu et
696 al. (2015) with known mass proportions of end members in synthetic mixtures (EM*) of (a) SD-MD, (b) SD-

V, and (c) V-MD magnetite particles, respectively. Solid lines are fits to the data using eqn. 6, which yield f = 2.72, 1.52, and 2.69, respectively.

Figure 5. FORC-PCA analysis of V-MD mixtures using the new unmixing algorithm. (**a-b**) Reconstructed FORC diagrams for EM1 (V) and EM2 (MD). (**c-d**) Reconstructed FORCs for EM1 and EM2. (**e**) PC score plot for a binary unmixing space between EM1 and EM2 (indicated by arrows). Diamonds illustrate the scores of individual samples. (**f**) Comparison of mixing proportions extracted using the new algorithm with the known mass proportions of end members in the synthetic mixture. The solid line indicates a one-to-one relationship.

Figure 6. FORC-PCA analysis of MD-SD mixtures using the new algorithm. (**a-c**) Reconstructed FORC diagrams for EM1 (MD), EM2 (SD high coercivity), and SD (low coercivity), respectively. (**d-f**) Reconstructed FORCs for EM1, EM2, and EM3, respectively. (**g**) PC score plot for a ternary unmixing space between EM1, EM2, and EM3 (black triangle). Diamonds illustrate the scores of individual samples. Contour lines represent the combined feasibility metric, *m*, for the saturation, monotonicity, and crossing metrics. (**h**) Comparison of mixing proportions extracted using the new algorithm with the known mass proportions of end members in the synthetic mixture. The solid line represents a one-to-one relationship.

Figure 7. FORC-PCA analysis of V-SD mixtures using the new algorithm. (**a-c**) Reconstructed FORC diagrams for EM1 (V), EM2 (SD high coercivity) and SD (low coercivity), respectively. (**d-f**) Reconstructed FORCs for EM1, EM2, and EM3, respectively. (**g**) PC score plot for a ternary unmixing space between EM1, EM2, and EM3 (black triangle). Diamonds illustrate the scores of individual samples. Contour lines represent the combined feasibility metric for the saturation, monotonicity, and crossing metrics. (**h**) Comparison of mixing proportions extracted using the new algorithm with the known mass proportions of end members in the synthetic mixture. The solid line represents a one-to-one relationship.

Figure 8. FORC-PCA analysis of greigite-bearing clay samples from the Tiber River, Rome (Florindo et al. (2007). (**a-c**) Reconstructed FORC diagrams for EM1 (moderately interacting SD greigite), EM2 (strongly interacting SD greigite) and EM3 (SP/SD greigite), respectively. (**d-f**) Reconstructed FORCs for EM1, EM2,

and EM3. The arrow in (f) indicates the downward-inflected response at the start of each FORC. Although this phenomenon is associated partially here with viscous SP behavior (Pike et al., 2001b), it is also likely to be partially an instrumental artefact in this case. (**g**) PC score plot for a ternary unmixing space between EM1, EM2, and EM3 (black triangle). Diamonds illustrate the scores of individual samples. Contour lines represent the combined feasibility metric for the saturation, monotonicity, and crossing metrics. The inset is an illustration of contours for the positivity metric. (**h**) Ternary diagram for the extracted proportions of EM1, EM2, and EM3. The blue line illustrates the two dominant mixing trends (EM3-EM2 and EM2-EM1). An example experimental FORC diagram for a mixture of strongly interacting and ~35% viscous SP/SD greigite is indicated by the arrow.

Figure 1.

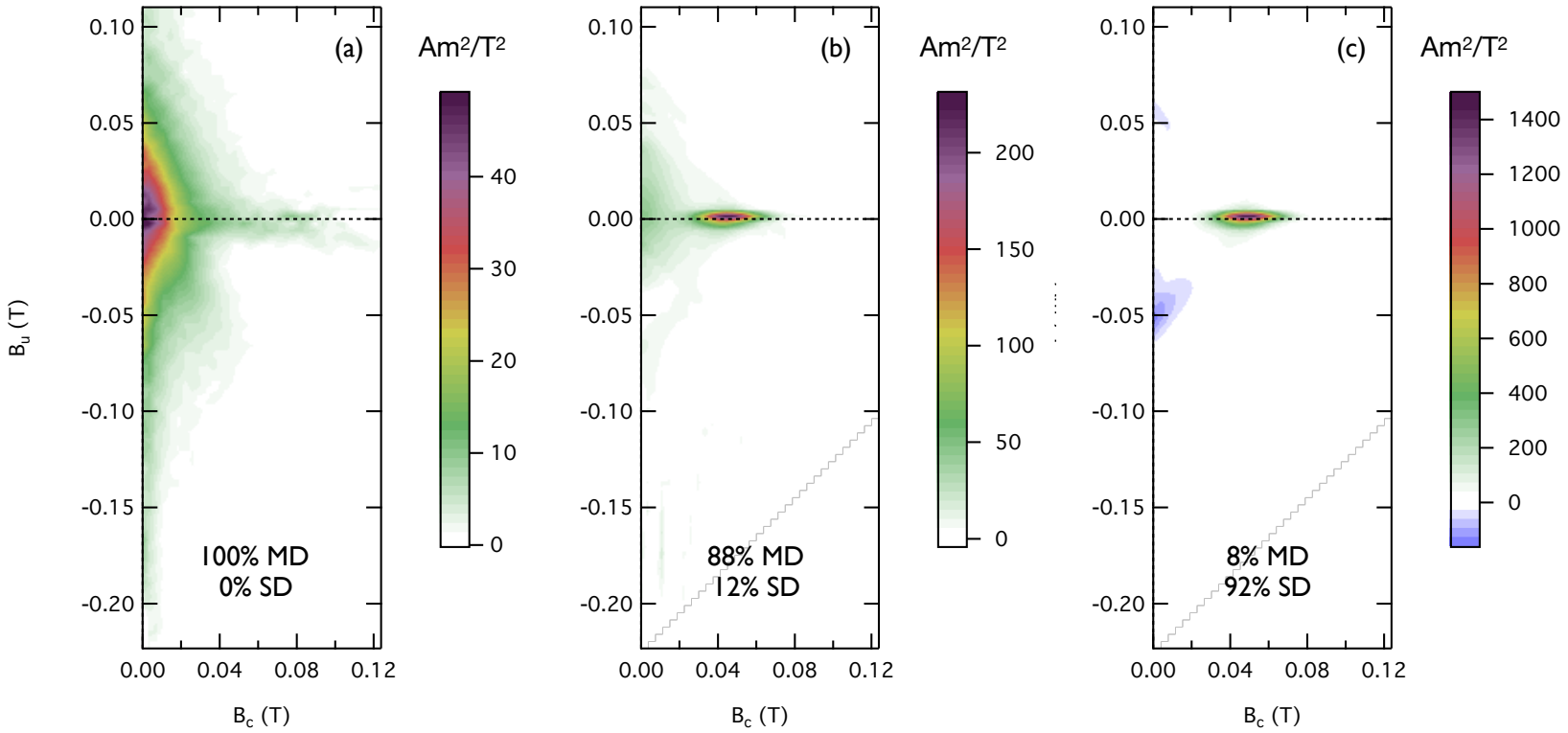
(a)
100% MD
0% SD
(b)
88% MD
12% SD
(c)
8% MD
92% SD
Am²/T²
B_u (T)
B_c (T)
0.10
0.05
0.00
-0.05
-0.10
-0.15
-0.20
0.00
0.04
0.08
0.12
0
10
20
30
40
50
100
150
200
400
600
800
1000
1200
1400

Figure 2.

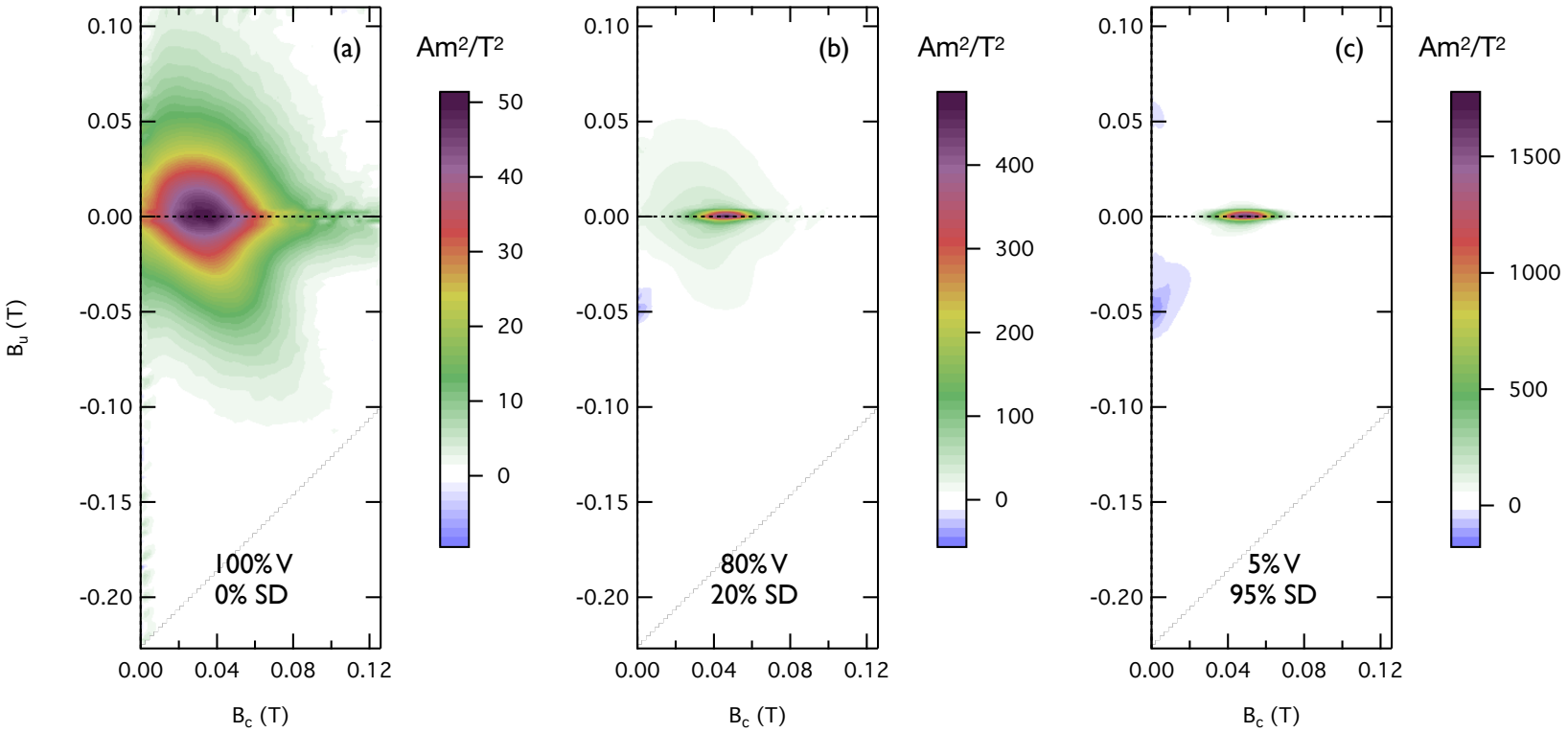
(a)
Am²/T²
50
40
30
20
10
0
100% V
0% SD
(b)
Am²/T²
400
300
200
100
0
80% V
20% SD
(c)
Am²/T²
1500
1000
500
0
5% V
95% SD
0.10
0.05
0.00
-0.05
-0.10
-0.15
-0.20
0.00
0.04
0.08
0.12
B_u (T)
B_c (T)

Figure 3.

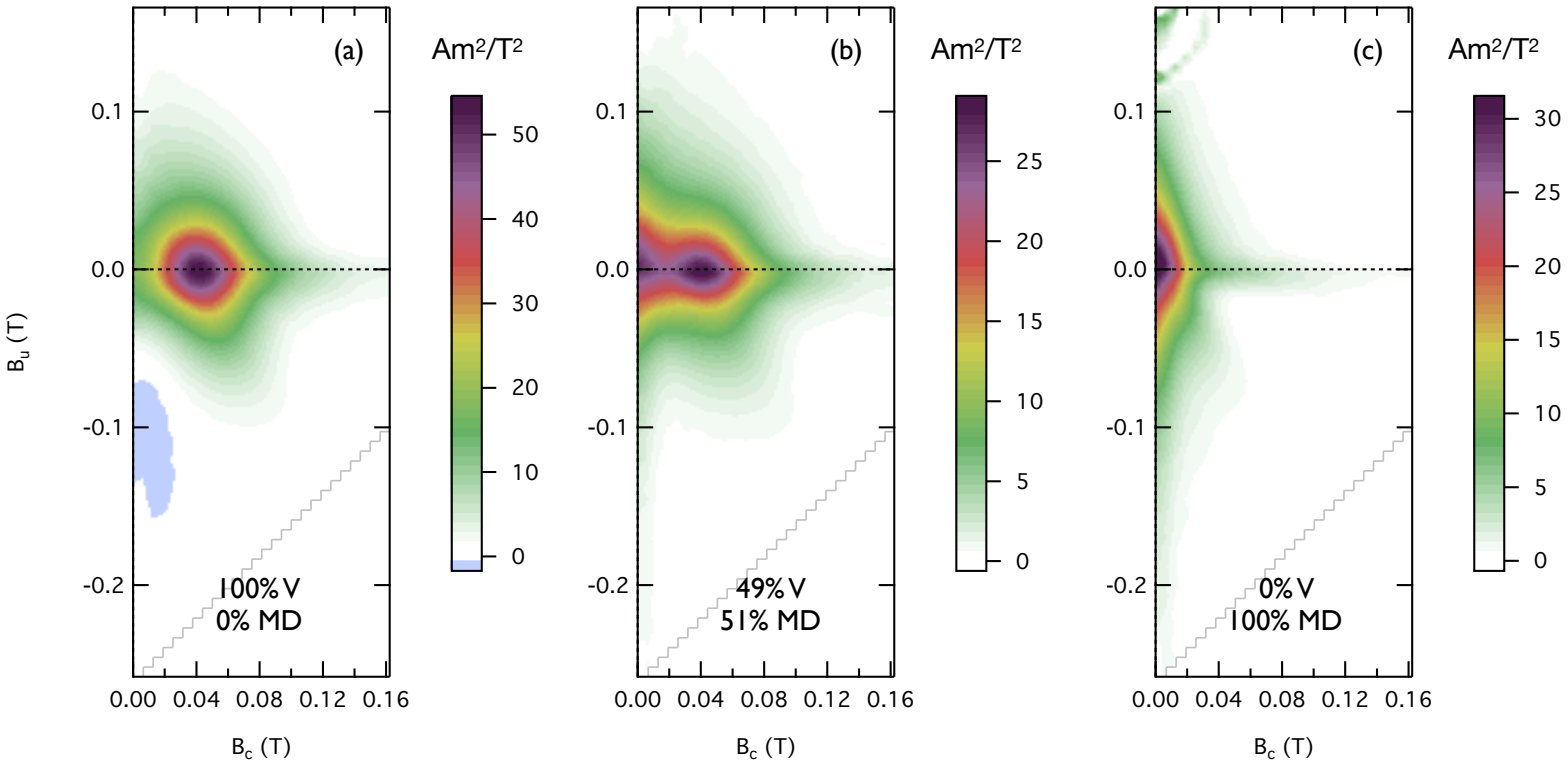
(a)
Am²/T²
100% V
0% MD
(b)
Am²/T²
49% V
51% MD
(c)
Am²/T²
0% V
100% MD
B_u (T)
B_c (T)
0.1
0.0
-0.1
-0.2
0.00 0.04 0.08 0.12 0.16
50 40 30 20 10 0
25 20 15 10 5 0
30 25 20 15 10 5 0

Figure 4.

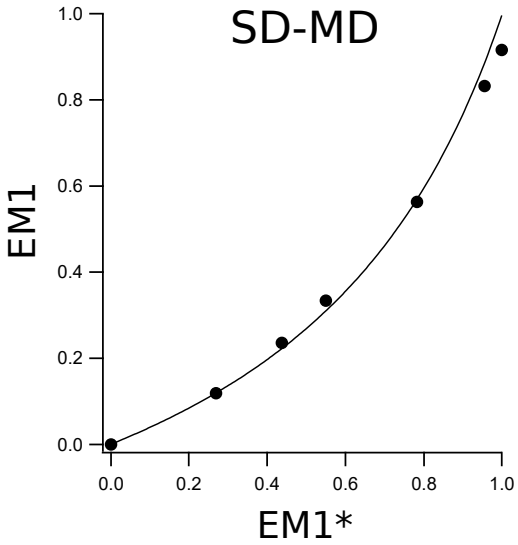
SD-MD
EM1
EM1*
0.0
0.2
0.4
0.6
0.8
1.0

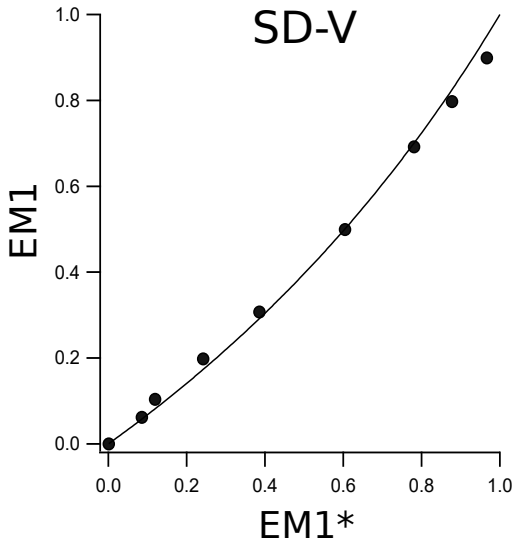
SD-V
EM1
EM1*
0.0
0.2
0.4
0.6
0.8
1.0

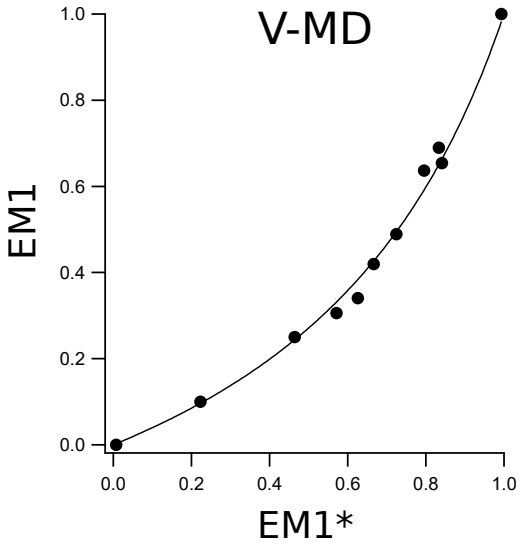
V-MD
EM1
EM1*
0.0
0.2
0.4
0.6
0.8
1.0

Figure 5.

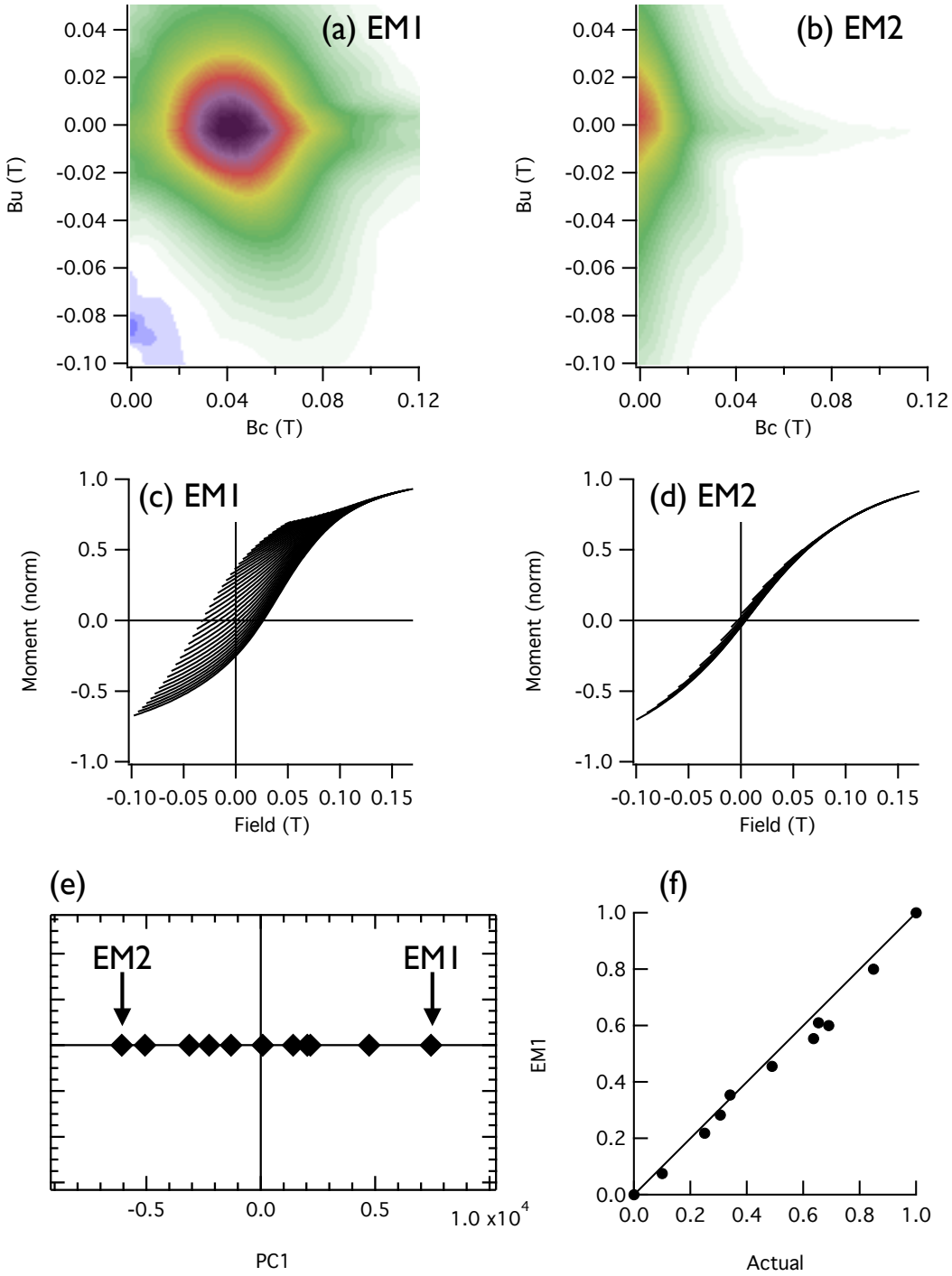
(a) EM1
(b) EM2
Bu (T)
Bc (T)
0.04
0.02
0.00
-0.02
-0.04
-0.06
-0.08
-0.10
0.00
0.04
0.08
0.12
(c) EM1
(d) EM2
Moment (norm)
1.0
0.5
0.0
-0.5
-1.0
-0.10 -0.05 0.00 0.05 0.10 0.15
Field (T)
(e)
EM2
EM1
-0.5
0.0
0.5
1.0 x10^4
PC1
(f)
EM1
Actual
0.0
0.2
0.4
0.6
0.8
1.0

Figure 6.

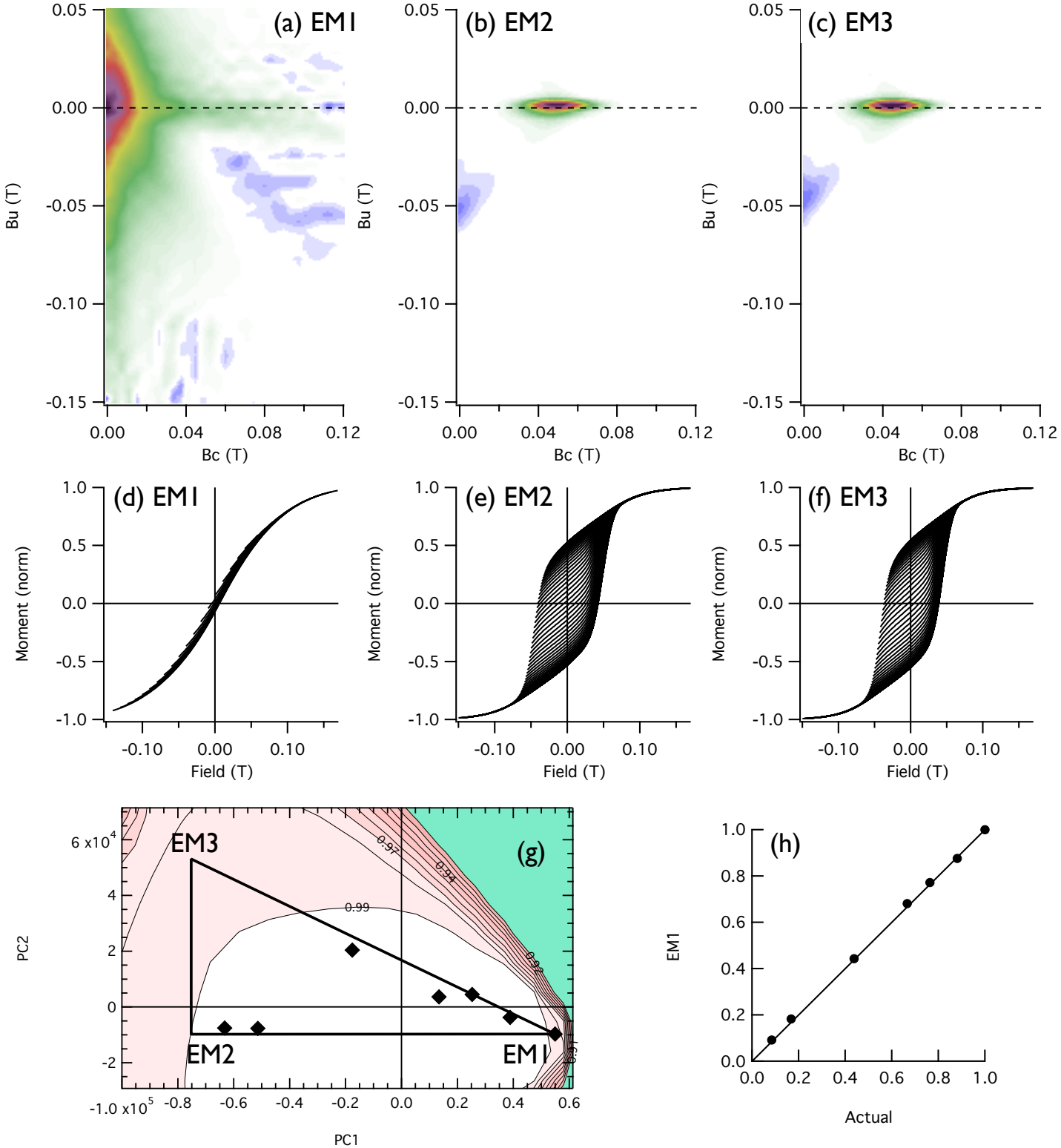
(a) EM1
(b) EM2
(c) EM3
Bu (T)
Bc (T)
0.05
0.00
-0.05
-0.10
-0.15
0.00
0.04
0.08
0.12
(d) EM1
(e) EM2
(f) EM3
Moment (norm)
Field (T)
1.0
0.5
0.0
-0.5
-1.0
-0.10
0.00
0.10
(g)
EM3
EM2
EM1
PC1
PC2
6 x10^4
4
2
0
-2
-1.0 x10^5
-0.8
-0.6
-0.4
-0.2
0.6
0.97
0.94
0.99
0.92
(h)
EM1
Actual
0.2
0.4
0.8
1.0

Figure 7.

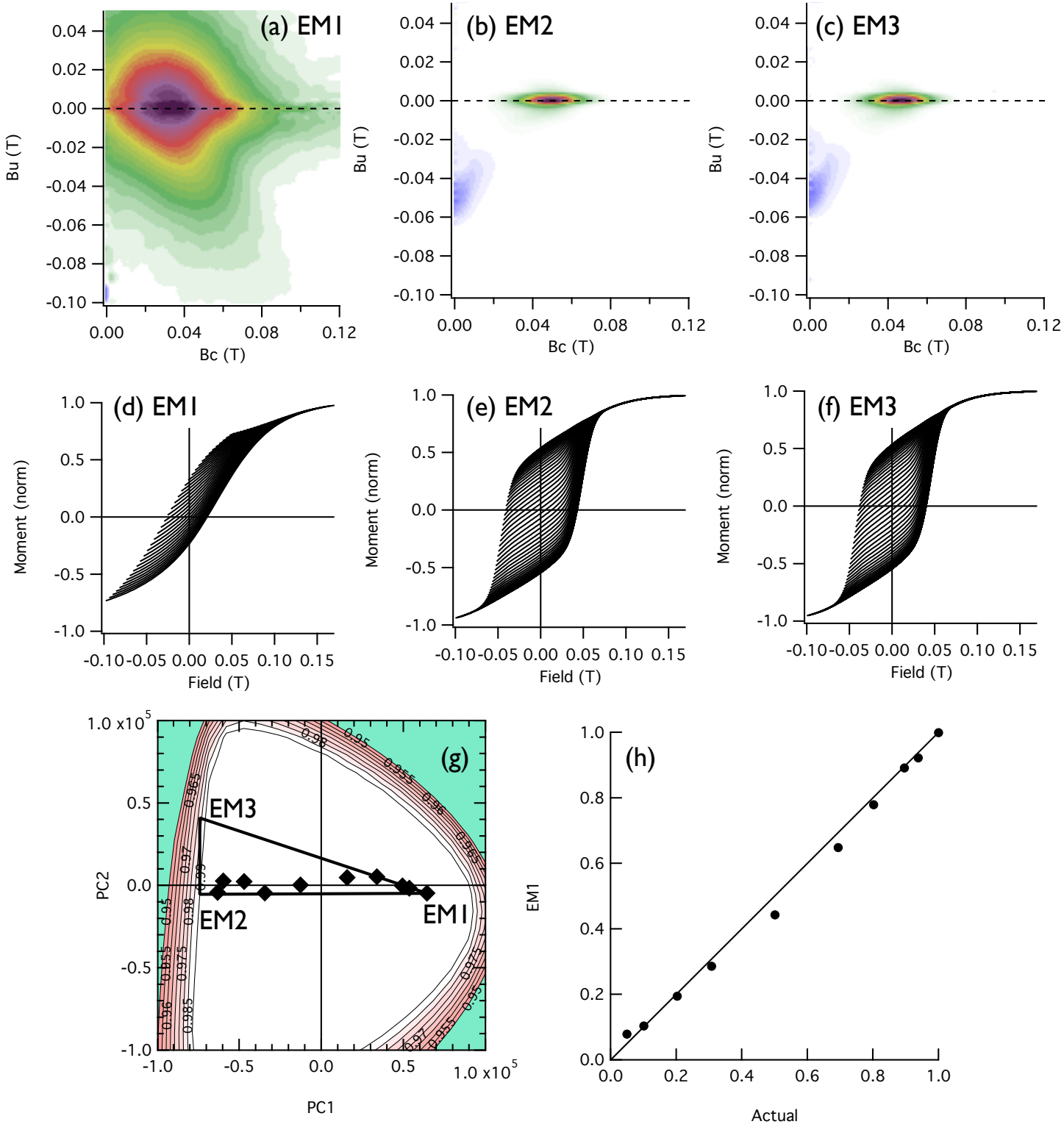
(a) EM1
(b) EM2
(c) EM3
Bu (T)
Bc (T)
(d) EM1
(e) EM2
(f) EM3
Moment (norm)
Field (T)
(g)
EM3
EM2
EM1
PC2
PC1
1.0 x10^5
(h)
EM1
Actual

Figure 8.

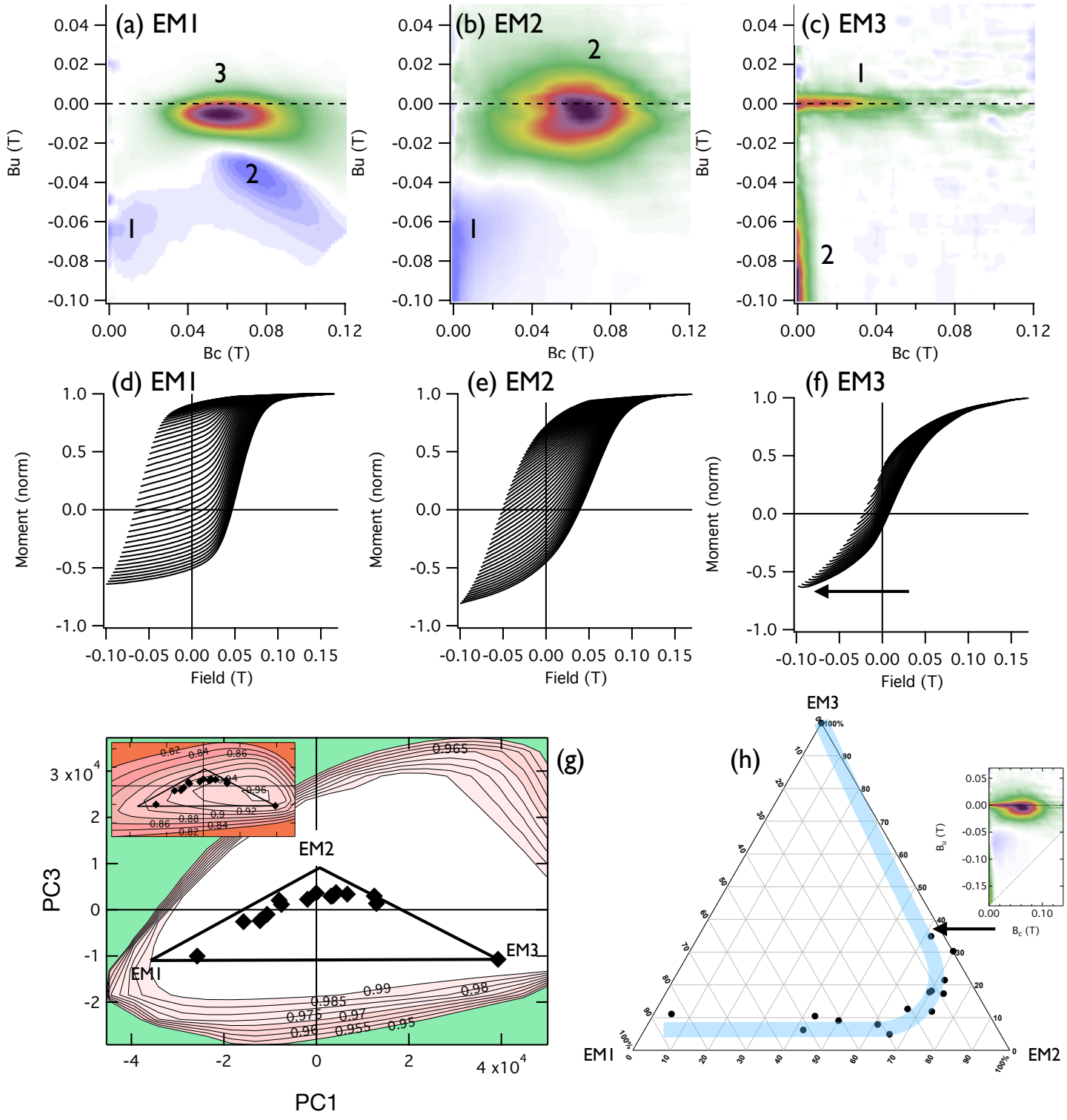
(a) EM1
(b) EM2
(c) EM3
Bu (T)
Bc (T)
(d) EM1
(e) EM2
(f) EM3
Moment (norm)
Field (T)
(g)
PC3
PC1
EM1
EM2
EM3
(h)
EM1
EM2
EM3
Bu (T)
Bc (T)

Table 1. Mass fractions of endmembers in measured samples			
Sample	SD	V	MD
V-MD			
wm_1		1.00	0.00
wm_2		0.85	0.15
wm_3		0.65	0.35
wm_4		0.64	0.36
wm_5		0.49	0.51
wm_6		0.69	0.31
wm_7		0.31	0.69
wm_8		0.34	0.66
wm_9		0.10	0.90
wm_10		0.00	1.00
wm_11		0.25	0.75
wm_12		0.42	0.58
SD-V			
w30_1	0.00	1.00	
w30_2	0.50	0.50	
w30_3	0.31	0.69	
w30_4	0.20	0.80	
w30_5	0.10	0.90	
w30_6	0.06	0.94	
w30_7	0.69	0.31	
w30_8	0.80	0.20	
w30_9	0.90	0.10	
w30_10	0.95	0.05	
SD-MD			
w14_1	0.00		1.00
w14_2	0.56		0.44
w14_3	0.33		0.67
w14_4	0.24		0.76
w14_5	0.12		0.88
w14_6	0.83		0.17
w14_7	0.92		0.08

Table 2. Summary of hysteresis properties for measured samples				
Sample	H_c (mT)	H_{cr} (mT)	H_{cr}/H_c	M_r/M_s
V-MD				
wm_1	31.35	52.56	1.68	0.29
wm_2	28.61	52.23	1.83	0.26
wm_3	23.11	79.32	3.43	0.20
wm_4	21.05	49.43	2.35	0.19
wm_5	18.25	48.59	2.66	0.16
wm_6	22.89	48.59	2.12	0.20
wm_7	13.70	46.04	3.36	0.12
wm_8	15.18	46.82	3.08	0.13
wm_9	2.59	34.53	13.36	0.03
wm_10	4.39	23.70	5.40	0.04
wm_11	11.11	42.61	3.83	0.09
wm_12	16.35	47.93	2.93	0.14
SD-V				
w30_1	24.20	45.26	1.87	0.02
w30_2	41.17	52.96	1.29	0.35
w30_3	35.85	52.79	1.47	0.29
w30_4	31.75	52.11	1.64	0.26
w30_5	27.55	50.56	1.84	0.23
w30_6	26.63	50.01	1.88	0.23
w30_7	41.34	49.42	1.20	0.40
w30_8	41.62	48.71	1.17	0.43
w30_9	41.78	48.63	1.16	0.47
w30_10	41.88	47.61	1.14	0.48
SD-MD				
w14_1	5.47	26.11	4.77	0.04
w14_2	34.24	49.43	1.44	0.27
w14_3	21.26	48.75	2.29	0.16
w14_4	16.52	47.85	2.90	0.13
w14_5	10.57	44.81	4.24	0.09
w14_6	41.45	49.35	1.19	0.40
w14_7	42.80	49.49	1.16	0.45

Table 3. Summary of hysteresis properties for extracted EMs				
V-MD				
	H_c (mT)	H_{cr}	H_{cr}/H_c	M_r/M_s
EM1	33.0	52.6	1.6	0.38
EM2	4.6	24.5	5.3	0.044
V (obs)	31.0	52.9	1.7	0.37
MD (obs)	4.5	24.4	5.5	0.045
SD-V				
EM1	27.0	49.0	1.8	0.34
EM2	42.0	48.0	1.1	0.54
EM3	39.0	45.0	1.2	0.54
SD (95%)	41.0	48.0	1.2	0.52
V (obs)	24	48.5	2.0	0.34
SD-MD				
EM1	6.0	26.8	4.5	0.07
EM2	41.0	47.5	1.2	0.53
EM3	37.5	43.5	1.2	0.55
SD (92%)	39.7	47.5	1.2	0.49
MD (obs)	5.2	26.9	5.1	0.07